

See discussions, stats, and author profiles for this publication at: <https://www.researchgate.net/publication/51647858>

Single-Nanopore Investigations with Ion Conductance Microscopy

ARTICLE *in* ACS NANO · SEPTEMBER 2011

Impact Factor: 12.88 · DOI: 10.1021/nn203205s · Source: PubMed

CITATIONS

20

READS

51

3 AUTHORS:



Chiao-Chen Chen

Indiana University Bloomington

13 PUBLICATIONS 181 CITATIONS

SEE PROFILE



Yi Zhou

Indiana University Bloomington

10 PUBLICATIONS 114 CITATIONS

SEE PROFILE



Lane A Baker

Indiana University Bloomington

90 PUBLICATIONS 2,492 CITATIONS

SEE PROFILE

Single-Nanopore Investigations with Ion Conductance Microscopy

Chiao-Chen Chen, Yi Zhou, and Lane A. Baker*

Department of Chemistry, Indiana University, 800 E. Kirkwood Avenue, Bloomington, Indiana 47405, United States

As the size of a pore shrinks, new physical properties can be observed due to the high surface area–volume relationship.¹ Particularly at the nanoscale, the electrical double layer,^{2–5} surface conductivities,^{6–8} and geometric asymmetry^{9,10} can result in new properties not observed at larger scales. Studies of transport at these small scales—particularly at the level of single nanopores—are fertile ground to develop deeper knowledge of the fundamentals of physical and biophysical processes.^{11–13} Further, applications of nanopores in the venues of chemical separations^{14–17} and sensor development^{18–22} promise advances in fields as diverse as genetic sequencing^{23–27} and fuel cells.^{28–32} Thus, new tools to study nanopores and nanoscale transport may find significant impact in the realm of both fundamental and applied sciences. Previous applications of scanning probe microscopies to the study of nanopores have demonstrated utility in determination of conductivity pathways and measurement of local concentrations or conductivities in the vicinity of the nanopore.^{33–39} Herein, we describe a modified three-electrode ion conductance microscope and demonstrate measurement of the properties of a single pore. With this configuration, the current–voltage properties of individual pores can be interrogated while scanning or at fixed positions. Measurements of the conductance properties of a single cylindrical pore and a single conical pore are demonstrated.

Scanning ion conductance microscopy (SICM) scans the surface of a sample with a nanometer scale pipet (nanopipet), often to collect topographic information in a non-invasive fashion.^{40–45} In SICM, the position of the pipet is controlled by carefully monitoring a small gap between the sample and pipet. The resistance of this gap (termed an access resistance) is a strong function of tip–sample separation and provides a method for feedback.^{46–50} In addition to

ABSTRACT A three-electrode scanning ion conductance microscope (SICM) was used to investigate the local current–voltage properties of a single nanopore. In this experimental configuration, the response measured is a function of changes in the resistances involved in the pathways of ion migration. Single-nanopore membranes utilized in this study were prepared with an epoxy painting procedure to isolate a single nanopore from a track-etch multipore membrane. Current–voltage responses measured with the SICM probe in the vicinity of a single nanopore were investigated in detail and agreed well with equivalent circuit models proposed in this study. With this modified SICM, the current–voltage responses characterized for the case of a single cylindrical pore and a single conical pore exhibit distinct conductance properties that originate from the geometry of nanopores.

KEYWORDS: microscopy · nanopore · conductance · membrane and ion transport

feedback control, under certain imaging conditions or scanning modes, ion currents from the pipet can also be monitored directly to characterize properties of the sample.^{41,51–54}

Here, membranes with single pores (cylindrical and conical in shape) have been prepared *via* the track-etch method.⁵⁵ A modified scanning ion conductance microscope with an additional electrode that serves to drive ions through this single pore is employed to examine nanopore conductivity. We find that for the case of a single pore this three-electrode system results in a predictable interaction between the electrode of the SICM and the working electrode of the nanopore. Advantages of this three-electrode configuration over a more conventional two-electrode SICM include independent control of the cross-membrane potential and enhanced contrast in the measurement of nanopore conductance. (A detailed description of the experimental advantages is provided in the Supporting Information.) Further, through careful control of pipet position (relative to the membrane pore) and control of the working electrode potential, the current–voltage response for the pore in the membrane can be measured with the pipet. Nanopipets were also capable of “dipping into” membrane pores, to operate within the pore itself.⁵⁶

* Address correspondence to
lanbaker@indiana.edu.

Received for review August 19, 2011
and accepted September 17, 2011.

Published online
10.1021/nn203205s

© XXXX American Chemical Society

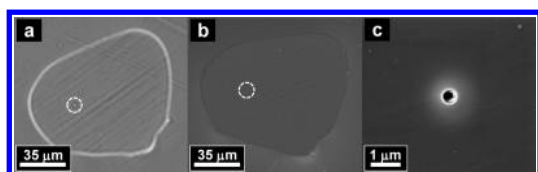


Figure 1. Optical (a) and SEM (b, c) images of a representative prepared single cylindrical pore membrane. The large oval shape observed in the optical image (a) indicates the boundary of the epoxy painting, inside of which the membrane can be exposed to electrolyte from both sides. White dashed circles on (a, b) indicate the locations of the isolated nanopores on the membrane. The pore diameter of the isolated cylindrical pore (c) shown here was characterized as 542 nm.

A model electrical circuit is proposed that predicts the observed response. Additional finite element simulations further confirm the proposed mechanism. The response for a cylindrical pore is described in detail, and measurement of a conical nanopore with rectified current flow is demonstrated. These preliminary results demonstrate that this three-electrode SICM provides a platform to characterize individual nanopores independent of other structures involved in the same system. Ultimately, this tool will provide a method to monitor nanopores in more complex biological and sensing environments.

RESULTS AND DISCUSSION

Current–Voltage Responses Measured with Modified SICM.

Single nanopores were isolated, and optical and electron micrographs of one such pore are shown in Figure 1. Effects of cross-membrane potentials on the topography and current images measured by SICM for single-nanopore membranes were recorded with distance-modulated (ac) feedback. The modified three-electrode SICM employed (Figure 2) allows for independent potential control of the working electrode (WE) and pipet electrode (PE), as referenced to a common reference electrode (RE). For all experiments reported in this study, the PE was held at +0.1 V and the RE served as ground. Topography and the corresponding current images obtained with three different working electrode potentials (+0.3, 0, and −0.3 V) are shown in Figure 3. Comparison of these three current images reveals that when the nanopipet scans over a pore, a negative working electrode potential (−0.3 V applied here) increases the potential drop across the PE and thus produces an increase in the pipet current. This results in an enhancement (greater current) of the ion current image that is obtained by plotting the changes in pipet current (ΔI) in x – y coordinates, as shown in Figure 3c. In contrast, when the WE was held at +0.3 V, the magnitude of the current image (ΔI) reduced to negative values (Figure 3d), as a result of reduction in the pipet currents due to the decrease of the voltage drop across the PE.

To better investigate the effect of the migration currents on the pipette currents under various working

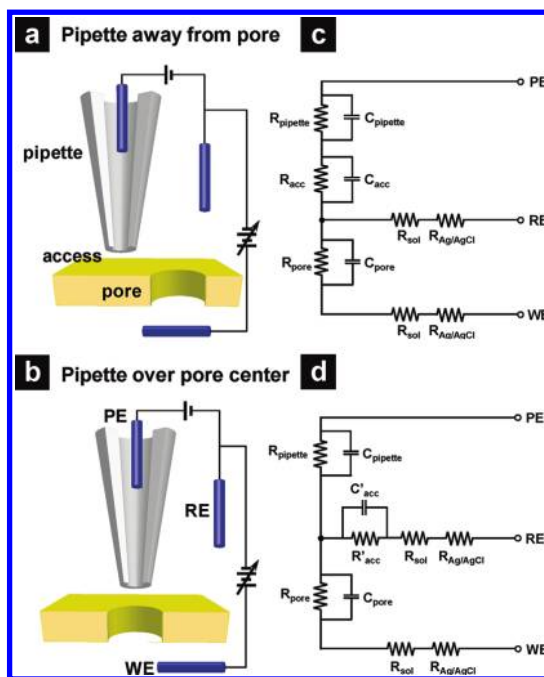


Figure 2. Schematic (a, b) of the relative positions of an SICM probe to a single pore membrane mounted on a perfusion cell. When the SICM probe is away from the pore center (a), the corresponding equivalent circuit (c) involves an access resistance, R_{acc} , generated from the probe–sample separation. In contrast, when the SICM is positioned over the pore center (b), another access resistance, R'_{acc} , results from the gap between the borders of the nanopore and the outer edge of the glass wall of the nanopipet and is present in the equivalent circuit (d). PE: pipet electrode, RE: reference electrode, and WE: working electrode.

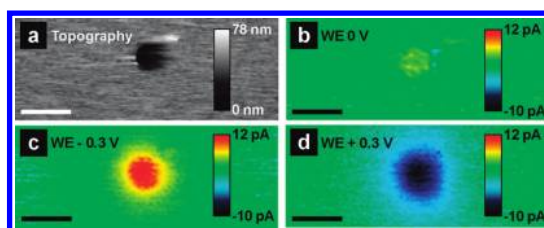


Figure 3. Topography (a) and the corresponding current images (b, c, d) of an isolated single nanopore measured with the three-electrode SICM described here. Images correspond to (b) 0 V, (c) −0.3 V, and (d) +0.3 V applied to the working electrode (WE). Scale bar: 1 μ m.

electrode potentials, instead of scanning the pipet, which can complicate the interpretation of recorded signals,^{51,52} ion currents were measured with the SICM probe at defined locations with the pipet in a fixed position. Figure 4a represents the relationship between the working electrode potential and currents measured at a vertical probe–sample distance (D_{ps}) of 170 nm. Here the probe is laterally positioned right over (Figure 4a, red ■) and far away (Figure 4a, ●) from the center of a single nanopore as a function of the potential applied to the WE. When the SICM probe was positioned over the pore center, the slope of the current–voltage response measured was about 10 times larger than that

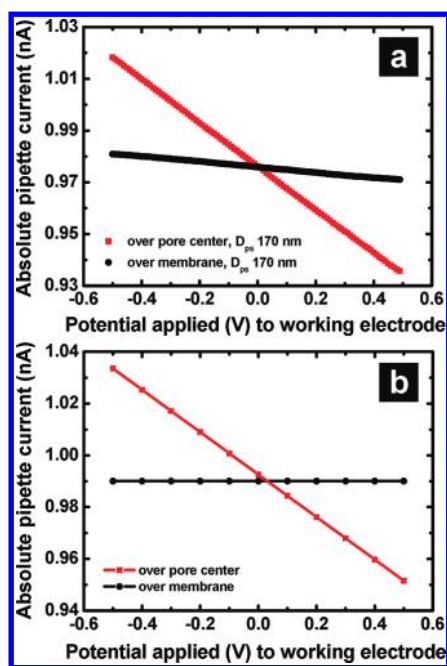


Figure 4. (a) Position-dependent current–voltage responses measured when the SICM probe was located over the pore center (red ■) and $8.5\ \mu\text{m}$ laterally away from the pore center (●). (b) Simulated data calculated from proposed equivalent circuit models.

obtained when the probe was located at a lateral displacement of $8.5\ \mu\text{m}$ away from the pore center.

This phenomenon is proposed to originate from changes in the resistance involved in the pathway of migration currents and can be explained well with the circuit models illustrated in Figure 2. To clarify, the access resistances R_{acc} and R'_{acc} in these two circuits have different arrangements and are related to different migration pathways. In Figure 2c, R_{acc} is the access resistance associated with the migration pathway between the WE and the PE due to the gap between the SICM probe and the membrane surface. However, when the nanopipet is positioned right over the pore center, the access resistance, R_{acc} , from the probe–sample distance is gone. R'_{acc} shown in Figure 2d, is generated from the migration pathway between the WE and the RE and results from the ring-shaped gap between the border of the nanopore and the outer edge of the glass wall of the nanopipet.

For the probe–sample distance of 170 nm utilized to obtain Figure 4a, the magnitudes of R_{acc} and R'_{acc} in the circuit models were estimated to be 1 and $0.75\ \text{M}\Omega$, respectively. Numerical values for R_{acc} and R'_{acc} at D_{ps} equal to 170 nm were assessed from approach curves. The approach curves were obtained by recording changes in the absolute pipet current as the probe was approached from bulk electrolyte to the membrane and to the pore center, respectively. For determination of access resistances, 0 V was applied to the WE. Typical values of R_{pipet} and R_{pore} are 100 and $86\ \text{M}\Omega$, respectively, as mentioned in the Experimental Section.

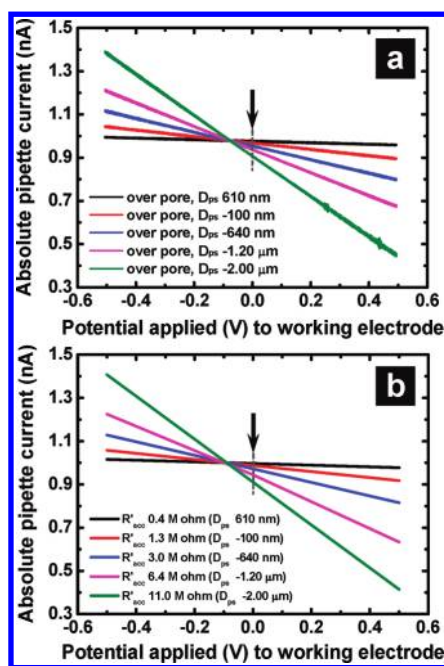


Figure 5. (a) Vertical distribution of the current–voltage responses characterized with three-electrode SICM over the center of a single cylindrical nanopore. (b) Simulated data produced from the equivalent circuit model shown in Figure 2d.

Compared to these resistances, additional resistances associated with the electrolyte solution (0.1 M KCl) and the charge transfer rate of Ag/AgCl electrodes, R_{sol} and $R_{Ag/AgCl}$, are typically negligible. Figure 4b represents the current–voltage responses simulated with the proposed circuit models, which fit well with the experimental data shown in Figure 4a. To further confirm observations of these position-dependent current–voltage responses detected and to estimate the capability of proposed equivalent circuit models, finite element method simulation was utilized to provide additional information (Supporting Information). Simulated results from finite element models (Figure S7) fit well with experimental measurements and predictions from the equivalent circuit models.

Spatial Distribution of Current–Voltage Responses. The current–voltage response through a single nanopore measured with an SICM probe in the vicinity of the pore opening displays a vertical distribution along the direction perpendicular to the membrane surface as shown in Figure 5a. Here, the absolute pipet current was recorded as a function of the potential applied to the WE at five selected probe–sample distances. Negative values of the D_{ps} mean that the probe (outer diameter of $\sim 250\ \text{nm}$, cone angle of $\sim 9.5^\circ$) was moved into the nanopore (pore diameter $\sim 500\ \text{nm}$). From these current–voltage responses, the effect of the applied potential on the measured pipet current became more apparent, especially when the probe was moved deeper into the pore center. When the probe moves into the pore, significant changes in the value of

the access resistance, R'_{acc} , are observed. This is likely a consequence of enhanced interactions between the charged walls of the pipet and the pore, similar to so-called “squeezing effects” observed in nanopore studies.^{40,57} A more direct evidence for the increase of R'_{acc} can be realized from the decrease in the absolute pipet current with the reduction of the probe–sample distance when the working electrode was maintained at 0 V (marked with black arrow in Figure 5a).

This vertical distribution of the current–voltage responses can be reproduced with the circuit model shown in Figure 2d, which describes the active components (resistors and capacitors) involved in the system when the nanopipet is positioned over the pore center. Numerical values of R'_{acc} utilized in the circuit model that correspond to various probe–sample distances were estimated on the basis of approach curves as described previously. Simulated data from the circuit model are illustrated in Figure 5b, where the current–voltage response of the greatest slope was obtained with the largest R'_{acc} and related to that recorded with the most negative D_{ps} shown in Figure 5a. In contrast, when the probe–sample separation is large ($D_{ps} = 610$ nm), the pipet current remained relatively constant independent of the potential applied to the WE due to the small access resistance ($R'_{acc} = 0.4$ M Ω).

In addition to vertical distribution, current–voltage responses measured with an SICM probe at a constant probe–sample distance also demonstrate dependence on lateral displacement from the pore center. Selected current–voltage (I – V) responses recorded from 0 to 8.55 μm away from the pore center at $D_{ps} = 170$ nm demonstrate a lateral distribution shown in Figure 6a. With consideration of the geometry of the SICM probe (i.d. ≈ 60 nm, o.d. ≈ 250 nm) and the single nanopore (~ 500 nm in diameter), the probe opening and the pore opening are completely overlapped (i.e., R_{acc} that results from the small probe–sample gap does not exist) at lateral displacements from 0 to 0.18 μm , and thus the behavior of I – V responses recorded are dominated by the access resistance, R'_{acc} , in the circuit model shown in Figure 2d (indicated as group 1 in Figure 6a). Responses measured at lateral displacements larger than 0.33 μm (classified as group 3 in Figure 6a) show similar and more gradual slopes. The behavior of these I – V responses can be explained with the circuit model illustrated in Figure 2c. Since the SICM probe was far from the single nanopore, the access resistance, R_{acc} , depends on the nanoscale probe–sample gap only. For the current–voltage response recorded at the lateral displacement of 0.33 μm (group 2 in Figure 6a), the tip opening of the SICM probe was moved away from the pore opening while the nanopipet still partially overlapped the single nanopore. Consequently, both R_{acc} and R'_{acc} affected the magnitude of pipet currents measured and thus

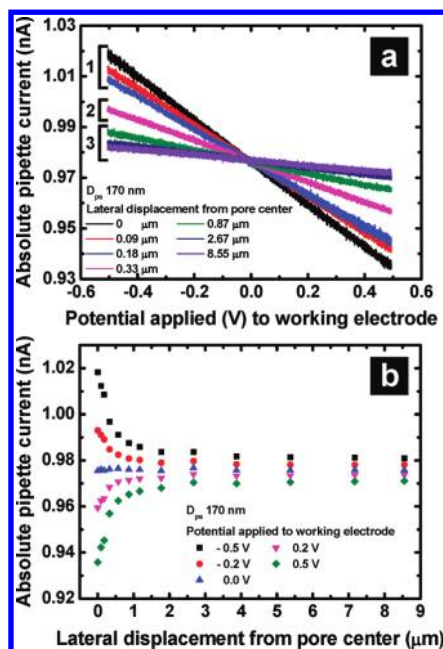


Figure 6. (a) Current–voltage responses measured with an SICM probe ($D_{ps} = 170$ nm) at different lateral displacements from the pore center. (b) Line profiles of the current magnitude measured at various applied potentials reconstructed from current–voltage responses recorded at different lateral displacements.

resulted in an I – V relationship located between the two extreme conditions in which the current–voltage responses were governed by only R_{acc} or R'_{acc} , respectively.

From the I – V responses recorded when the SICM probe was moved laterally away from the pore center, line profiles of the current magnitude measured at various applied potentials can be reconstructed. Figure 6b illustrates the reconstructed line profiles of the pipet current measured at five representative applied potentials. Potential applied to the WE results in the greatest changes in current magnitude when the nanopipet was located at the center of the single pore. In contrast, the magnitude of the currents measured was fairly constant under a given applied potential when the SICM probe was away from the pore center.

Characterization of Pore Geometry. In addition to the case of a single cylindrical pore examined in the experiments discussed above, the current–voltage response through a single conical pore was characterized with this three-electrode SICM as well. The single conical pore membrane was prepared by the epoxy painting method described in the Experimental Section, and a conical pore with a base diameter of 690 ± 25 nm ($n = 3$) and a tip diameter of 44 ± 8 nm ($n = 3$) was isolated for this experiment. The single conical pore membrane was mounted tip-side up on the perfusion cell in which the SICM probe was allowed to access the tip side of the conical pore.

Figure 7a shows pipet currents, measured over the center of the tip opening of the conical pore

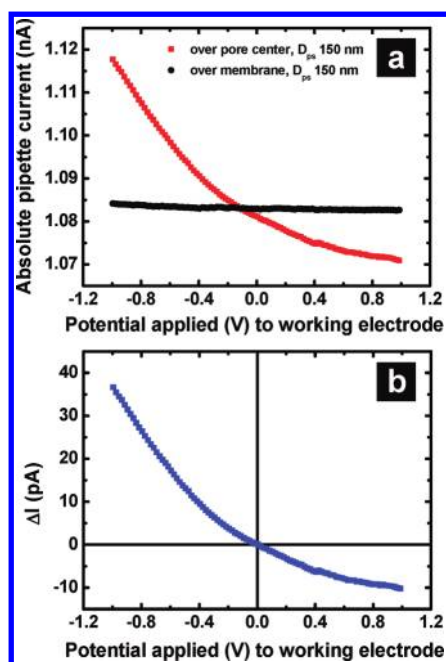


Figure 7. (a) Current–voltage responses recorded with an SICM probe for a single conical pore. When the SICM probe was located over the pore center, current rectification was observed (red ■). In contrast, the magnitude of the pipet current remained almost constant independent of the applied potential when the current–voltage response was measured 5 μm away from the pore center (●). (b) Changes in the absolute pipette current ($\Delta I = I_{\text{pipet,WE}} - I_{\text{pipet,WE}=0}$) recorded when the SICM probe was located over the pore center were plotted as a function of the potential applied to the working electrode.

(Figure 7a, red ■) and at a lateral displacement of 5.9 μm away from the pore center (Figure 7a, ●), as a function of the potential applied to the WE at a constant D_{ps} of 150 nm. From this plot, differences of current–voltage responses measured with SICM that depend on pipet position can also be observed with the conical pore membrane. Similar to a cylindrical pore membrane, the magnitude of the pipet current recorded far from the pore center remained almost independent of the potential applied. However, the current–voltage response recorded over the conical pore center (Figure 7a, red ■) showed a significant difference from that obtained with a cylindrical pore membrane (Figure 4a, red ■).

Conical nanopores exhibit rectified current flow, a consequence of the asymmetric pore geometry and the high surface to volume ratio of the tip. For conical nanopores with negative surface charge, a negative potential on the large (base) side of the pore results in greater currents (*i.e.*, higher pore conductance/lower pore resistance) than the case of the corresponding positive potential. (Supporting Information, Figure S2c). Here, membranes with a single, negatively charged conical nanopore were mounted tip-side up in the perfusion cell. The WE in the lower chamber faced the base side of the conical pore, with the RE in the upper chamber. Therefore, a greater migration current (*i.e.*,

higher pore conductance/lower pore resistance) through the conical pore was observed when the WE was held at a negative potential compared to the case in which the corresponding positive potential was applied. Furthermore, in the case of a single cylindrical pore, when the SICM probe was located over the pore center, a linear change in pipet current induced by the potential applied to the WE was observed. However, for the conical pore investigated here, due to the aforementioned rectification effect, the pore resistance is not constant but changes nonlinearly with the applied working electrode potential. This results in a curved (rectified) relationship between the absolute pipet currents measured and the potential applied to the WE.

Therefore, in contrast to the cylindrical pore, in which changes in the absolute pipet current ($\Delta I = I_{\text{pipet,WE}} - I_{\text{pipet,WE}=0}$) provide a linear relationship to the working electrode potential, ΔI of a conical pore displays a rectified response, as shown in Figure 7b. In addition, for a cylindrical pore, negative working electrode potentials result in a positive ΔI (increase in absolute pipet current), while a negative ΔI (decrease in absolute pipet current) was detected at positive working electrode potentials. The same phenomenon was observed for the conical pore. Consequently, the direction of current rectification shown in Figure 7b is reversed to that of the bulk current–voltage response determined with conventional macroscopic measurements shown in Figure S4c. Although the rectification direction is reversed, the rectification ratio observed from the nanopipet measurement ($|\Delta I_{-0.6\text{V}}/\Delta I_{+0.6\text{V}}| = 1.83$ from Figure 7b) is in good agreement with the result for the measurement of rectification ($|I_{-0.6\text{V}}/I_{+0.6\text{V}}| = 1.84$ from Figure S4c) of the conical nanopore membrane from the bulk.

Hence, the absolute pipet current recorded as a function of the potential applied to the WE displays a rectified current response that reflects the conical geometry of the nanopore under study. This result demonstrates that by examination of the current–voltage responses measured with an SICM probe, nanopores with distinct geometry can be identified.

CONCLUSION

In this study, we have developed a simple approach to prepare a single-nanopore membrane that utilizes water-resistive epoxy to isolate a single nanopore from a low-density track-etched polyimide membrane. This painting method allows preparation of single nanopore membranes without a complicated lithography procedure. In addition, a modified scanning ion conductance microscope with three electrodes has been established to investigate the effects of ion migration on the current magnitude measured at the vicinity of a single nanopore. Current–voltage responses detected

with an SICM probe showed spatial distributions that can be explained with equivalent circuit models purposed in this study. Furthermore, by comparing the characteristics of the current–voltage responses recorded for individual nanopores, nanopores with

distinct geometry can be distinguished from each other. Therefore, this three-electrode SICM provides a promising platform to study the heterogeneous multiple nanopore (nanochannel) systems found in materials and biological settings.

EXPERIMENTAL SECTION

Chemicals and Materials. Solutions were prepared with deionized water (resistivity = 18 M Ω ·cm) obtained from a Milli-Q water purification system (Millipore Corp., Danvers, MA, USA). Sodium iodide (Mallinckrodt, Philipsburg, NJ, USA) and sodium hypochlorite (10–15% active chlorine, Sigma-Aldrich, St. Louis, MO, USA) were utilized to prepare nanoporous membranes as described previously.⁵⁵ Potassium chloride (Mallinckrodt) solutions with a concentration of 0.1 M were filtered with 0.22 μ m PVDF filter membranes (Millipore Corp.) and utilized as electrolyte for SICM measurements. Clear, water-resistive epoxy (Devcon, Riviera Beach, FL, USA) was applied to isolate a single nanopore in a membrane as described (*vide infra*).

Membrane Preparation and Characterization. Nanoporous membranes utilized in this study were prepared from low-density ion-tracked polyimide membranes (track density 10⁴ tracks/cm², thickness 25 μ m, it4ip, Belgium) via the track-etch process.⁵⁵ Immersion of ion-tracked membranes in active sodium hypochlorite solution (10–15%) at 70 °C for 15 min resulted in porous membranes containing cylindrical pores. To prepare membranes with conical pores, an ion-tracked membrane was mounted between two halves of a U-tube, in which etching solution (10–15% sodium hypochlorite solution) was filled in one-half and stop solution (1 M sodium iodide) was loaded in the other half. This U-tube with an ion-tracked membrane mounted was then placed in a water bath for 95 min at 50 °C.

Porous membranes prepared were mounted on a glass slide and placed on an inverted optical microscope (Nikon TE2000, Melville, NY, USA) where a water-resistive epoxy was applied to one side of the membrane to isolate a single nanopore (for a conical pore membrane, the epoxy painting was applied to the base side). To increase the strength of the membrane and allow the isolated single pore to contact the electrolyte solution on both sides, single-nanopore membranes were then masked further in clear tape.

Pore sizes of single nanopores were determined via current–voltage measurements and scanning electron microscopy (SEM, FEI Quanta-FEG) as described in the Supporting Information (Figure S2). Optical and SEM images of representative single-nanopore membranes are shown in Figure 1. Figure 1c shows an electron micrograph of a cylindrical pore from an isolated single-pore membrane postexamination by scanning ion conductance microscopy. Minor salt deposits that remain on the inner surface of the nanopore can be observed. For the single cylindrical pore membranes utilized in this study, the pore diameter was characterized as 462 \pm 35 nm (n = 6). For the single conical pore membranes applied here, pore resistance was determined with current–voltage measurements, and the base diameter was characterized to be 690 \pm 25 nm (n = 3) with SEM. As described in the Supporting Information, the pore tip diameter was determined to be 44 \pm 8 nm (n = 3).

Instrumentation and the Equivalent Circuits for the Experimental Setup. Data were acquired with a ScanIC scanning ion conductance microscope (ionscope, Ltd., London, UK) in conjunction with an Axopatch 200B current amplifier (Molecular Devices, Union City, CA). SICM operated in both nonmodulated (dc) and distance-modulated (ac) modes has been described previously.^{41–43,58} Briefly, the SICM probe consists of a nanopipet filled with electrolyte (0.1 M KCl) and back inserted with a Ag/AgCl electrode. A Ag/AgCl reference electrode is placed in the bath electrolyte, and a constant potential is applied between the pipet and the reference electrodes. The SICM probe is

mounted on a three-dimensional piezoactuator integrated with a dc motor to control pipet position.

To investigate the effect of ion migration through a single nanopore on current measured by SICM, a third Ag/AgCl electrode was placed in the lower chamber of the perfusion cell (Figure 2). The perfusion cell consists of a single-nanopore membrane mounted between the upper and the lower chambers of the cell, which are filled with 0.1 M KCl. Pipet and reference electrodes reside in the upper chamber. Potential applied to the PE was maintained at +0.1 V, while the RE was grounded to a faraday cage. Potential applied to the WE in the bottom chamber was controlled by a function generator (Agilent 33220A, Loveland, CO, USA) to produce a defined cross-membrane potential. This experimental setup is illustrated in Figure 2, which depicts the case of two representative positions of a nanopipet. Current–voltage responses are detected with the SICM probe at a constant probe–sample distance. In Figure 2a, the nanopipet is far away from the center of the single nanopore, and the circuit model utilized to describe the components involved in this configuration is shown in Figure 2c. Figure 2b illustrates the situation when a nanopipet is located over the pore center, and the associated circuit model is depicted in Figure 2d.

In both circuit models, R_{pipet} is the pipet resistance determined by the geometry of the SICM probe, which is typically around 100 M Ω for the glass nanopipets utilized in this experiment. The inner and outer diameters of these nanopipets are about 60 and 250 nm (Figure S3), respectively. R_{acc} and R'_{acc} are the access resistances associated with each configuration; the magnitudes of each are affected by both the probe–sample distance and the surface topography of the specimen. R_{pore} represents the resistance of the nanopore, which is about 86.0 \pm 12.1 M Ω (n = 6) for the single-pore membranes prepared for this experiment. R_{sol} and $R_{\text{Ag/AgCl}}$ are the resistances associated with the electrolyte solution (0.1 M KCl) and the charge transfer rate of the Ag/AgCl electrodes, whose magnitudes are typically negligible compared to the other resistances involved in the system. In addition, C_{pipet} , C_{acc} , C'_{acc} , and C_{pore} represent the capacitive components due to the high surface to volume ratios of the nanopipet, the single nanopore, and the nanoscale probe–sample gap, respectively.

Acknowledgment. This work was supported by National Institutes of Health (NIDDK 1R21DK082990), Research Corporation for Scientific Advancement (Cottrell Scholars Award), and the American Heart Association (Scientist Development Grant). The authors greatly appreciate valuable discussions and technical support concerning electronic instrumentation from Mr. Andy Alexander and Mr. John Poehlman. We are also grateful to Mr. Joseph Basore for suggestions about pore isolation and Mr. Maksymilian A. Derylo for comments.

Supporting Information Available: Comparison of the characteristics between three-electrode SICM reported here and the conventional two-electrode SICM system is discussed. In addition, characterizations of nanopipets and single-nanopore membranes utilized here as well as the finite element method modeling for three-electrode SICM are described. This material is available free of charge via the Internet at <http://pubs.acs.org>.

REFERENCES AND NOTES

- Schoch, R. B.; Han, J.; Renaud, P. Transport Phenomena in Nanofluidics. *Rev. Mod. Phys.* **2008**, *80*, 839–883.

2. Dutta, P.; Beskok, A. Analytical Solution of Combined Electroosmotic/Pressure Driven Flows in Two-Dimensional Straight Channels: Finite Debye Layer Effects. *Anal. Chem.* **2001**, *73*, 1979–1986.
3. Pu, Q.; Yun, J.; Temkin, H.; Liu, S. Ion-Enrichment and Ion-Depletion Effect of Nanochannel Structures. *Nano Lett.* **2004**, *4*, 1099–1103.
4. Pennathur, S.; Santiago, J. G. Electrokinetic Transport in Nanochannels. 1. Theory. *Anal. Chem.* **2005**, *77*, 6772–6781.
5. Pennathur, S.; Santiago, J. G. Electrokinetic Transport in Nanochannels. 2. Experiments. *Anal. Chem.* **2005**, *77*, 6782–6789.
6. van der Heyden, F. H. J.; Stein, D.; Dekker, C. Streaming Currents in a Single Nanofluidic Channel. *Phys. Rev. Lett.* **2005**, *95*, 116104.
7. Nguyen, G.; Vlassioulak, I.; Siwy, Z. S., Comparison of Bipolar and Unipolar Ionic Diodes. *Nanotechnology* **2010**, *21*.
8. Plecis, A.; Nanteuil, C. m.; Haghir-Gosnet, A.-M.; Chen, Y. Electropreconcentration with Charge-Selective Nanochannels. *Anal. Chem.* **2008**, *80*, 9542–9550.
9. Kubeil, C.; Bund, A. The Role of Nanopore Geometry for the Rectification of Ionic Currents. *J. Phys. Chem. C* **2011**, *115*, 7866–7873.
10. Cheng, L. J.; Guo, L. J. Nanofluidic Diodes. *Chem. Soc. Rev.* **2010**, *39*, 923–938.
11. Duan, C. H.; Majumdar, A. Anomalous Ion Transport in 2-nm Hydrophilic Nanochannels. *Nat. Nanotechnol.* **2010**, *5*, 848–852.
12. Hou, X.; Guo, W.; Jiang, L. Biomimetic Smart Nanopores and Nanochannels. *Chem. Soc. Rev.* **2011**, *40*, 2385–2401.
13. Hou, X.; Yang, F.; Li, L.; Song, Y. L.; Jiang, L.; Zhu, D. B. A Biomimetic Asymmetric Responsive Single Nanochannel. *J. Am. Chem. Soc.* **2010**, *132*, 11736–11742.
14. Han, J.; Craighead, H. G. Separation of Long DNA Molecules in a Microfabricated Entropic Trap Array. *Science* **2000**, *288*, 1026–1029.
15. Kuo, T. C.; Cannon, D. M.; Chen, Y. N.; Tulock, J. J.; Shannon, M. A.; Sweedler, J. V.; Bohn, P. W. Gateable Nanofluidic Interconnects for Multilayered Microfluidic Separation Systems. *Anal. Chem.* **2003**, *75*, 1861–1867.
16. Garcia, A. L.; Ista, L. K.; Petsev, D. N.; O'Brien, M. J.; Bisong, P.; Mammoli, A. A.; Brueck, S. R. J.; Lopez, G. P. Electrokinetic Molecular Separation in Nanoscale Fluidic Channels. *Lab Chip* **2005**, *5*, 1271–1276.
17. Fu, J. P.; Schoch, R. B.; Stevens, A. L.; Tannenbaum, S. R.; Han, J. Y. A Patterned Anisotropic Nanofluidic Sieving Structure for Continuous-Flow Separation of DNA and Proteins. *Nat. Nanotechnol.* **2007**, *2*, 121–128.
18. Fu, Y. Q.; Tokuhisa, H.; Baker, L. A. Nanopore DNA Sensors Based on Dendrimer-Modified Nanopipettes. *Chem. Commun.* **2009**, 4877–4879.
19. Sa, N. Y.; Fu, Y. Q.; Baker, L. A. Reversible Cobalt Ion Binding to Imidazole-Modified Nanopipettes. *Anal. Chem.* **2010**, *82*, 9963–9966.
20. Umehara, S.; Karhanek, M.; Davis, R. W.; Pourmand, N. Label-Free Biosensing with Functionalized Nanopipette Probes. *Proc. Natl. Acad. Sci. U. S. A.* **2009**, *106*, 4611–4616.
21. Actis, P.; Mak, A.; Pourmand, N. Functionalized Nanopipettes: Toward Label-Free, Single Cell Biosensors. *Bioanal. Rev.* **2010**, *1*, 177–185.
22. Ali, M.; Yameen, B.; Neumann, R.; Ensinger, W.; Knoll, W.; Azzaroni, O. Biosensing and Supramolecular Bioconjugation in Single Conical Polymer Nanochannels. Facile Incorporation of Biorecognition Elements into Nanoconfined Geometries. *J. Am. Chem. Soc.* **2008**, *130*, 16351–16357.
23. Kawano, R.; Schibel, A. E. P.; Cauley, C.; White, H. S. Controlling the Translocation of Single-Stranded DNA through alpha-Hemolysin Ion Channels Using Viscosity. *Langmuir* **2009**, *25*, 1233–1237.
24. Cockroft, S. L.; Chu, J.; Amarin, M.; Ghadiri, M. R. A Single-Molecule Nanopore Device Detects DNA Polymerase Activity with Single-Nucleotide Resolution. *J. Am. Chem. Soc.* **2008**, *130*, 818–820.
25. Ashkenasy, N.; Sanchez-Quesada, J.; Bayley, H.; Ghadiri, M. R. Recognizing a Single Base in an Individual DNA Strand: A Step toward DNA Sequencing in Nanopores. *Angew. Chem., Int. Ed.* **2005**, *44*, 1401–1404.
26. Ma, L.; Cockroft, S. L. Biological Nanopores for Single-Molecule Biophysics. *ChemBioChem* **2010**, *11*, 25–34.
27. Schibel, A. E. P.; An, N.; Jin, Q.; Fleming, A. M.; Burrows, C. J.; White, H. S. Nanopore Detection of 8-Oxo-7,8-dihydro-2'-deoxyguanosine in Immobilized Single-Stranded DNA via Adduct Formation to the DNA Damage Site. *J. Am. Chem. Soc.* **2010**, *132*, 17992–17995.
28. Vichi, F. M.; Colomer, M. T.; Anderson, M. A. Nanopore Ceramic Membranes as Novel Electrolytes for Proton Exchange Membranes. *Electrochem. Solid State* **1999**, *2*, 313–316.
29. Pereira, F.; Vallé, K.; Belleville, P.; Morin, A.; Lambert, S.; Sanchez, C. Advanced Mesoscale Hybrid Silica Nafion Membranes for High-Performance PEM Fuel Cell. *Chem. Mater.* **2008**, *20*, 1710–1718.
30. Ioroi, T.; Kuraoka, K.; Yasuda, K.; Yazawa, T.; Miyazaki, Y. Surface-Modified Nanopore Glass Membrane as Electrolyte for DMFCs. *Electrochem. Solid State* **2004**, *7*, A394–A396.
31. Liu, S. R.; Pu, Q. S.; Gao, L.; Korzeniewski, C.; Matzke, C. From Nanochannel-Induced Proton Conduction Enhancement to a Nanochannel-Based Fuel Cell. *Nano Lett.* **2005**, *5*, 1389–1393.
32. Bussian, D. A.; O'Dea, J. R.; Metiu, H.; Buratto, S. K. Nanoscale Current Imaging of the Conducting Channels in Proton Exchange Membrane Fuel Cells. *Nano Lett.* **2007**, *7*, 227–232.
33. Bath, B. D.; Lee, R. D.; White, H. S.; Scott, E. R. Imaging Molecular Transport in Porous Membranes. Observation and Analysis of Electroosmotic Flow in Individual Pores Using the Scanning Electrochemical Microscope. *Anal. Chem.* **1998**, *70*, 1047–1058.
34. Bath, B. D.; White, H. S.; Scott, E. R. Electrically Facilitated Molecular Transport. Analysis of the Relative Contributions of Diffusion, Migration, and Electroosmosis to Solute Transport in an Ion-Exchange Membrane. *Anal. Chem.* **2000**, *72*, 433–442.
35. Ervin, E. N.; White, H. S.; Baker, L. A. Alternating Current Impedance Imaging of Membrane Pores Using Scanning Electrochemical Microscopy. *Anal. Chem.* **2005**, *77*, 5564–5569.
36. Ervin, E. N.; White, H. S.; Baker, L. A.; Martin, C. R. Alternating Current Impedance Imaging of High-Resistance Membrane Pores Using a Scanning Electrochemical Microscope. Application of Membrane Electrical Shunts to Increase Measurement Sensitivity and Image Contrast. *Anal. Chem.* **2006**, *78*, 6535–6541.
37. Gardner, C. E.; Unwin, P. R.; Macpherson, J. V. Correlation of Membrane Structure and Transport Activity Using Combined Scanning Electrochemical-Atomic Force Microscopy. *Electrochem. Commun.* **2005**, *7*, 612–618.
38. Uitto, O. D.; White, H. S. Scanning Electrochemical Microscopy of Membrane Transport in the Reverse Imaging Mode. *Anal. Chem.* **2001**, *73*, 533–539.
39. Uitto, O. D.; White, H. S.; Aoki, K. Diffusive-Convective Transport into a Porous Membrane. A Comparison of Theory and Experiment Using Scanning Electrochemical Microscopy Operated in Reverse Imaging Mode. *Anal. Chem.* **2002**, *74*, 4577–4582.
40. Bocker, M.; Muschter, S.; Schmitt, E. K.; Steinem, C.; Schaffer, T. E. Imaging and Patterning of Pore-Suspending Membranes with Scanning Ion Conductance Microscopy. *Langmuir* **2009**, *25*, 3022–3028.
41. Hansma, P. K.; Drake, B.; Marti, O.; Gould, S. A. C.; Prater, C. B. The Scanning Ion-Conductance Microscope. *Science* **1989**, *243*, 641–643.
42. Korchev, Y. E.; Bashford, C. L.; Milovanovic, M.; Vodyanoy, I.; Lab, M. J. Scanning Ion Conductance Microscopy of Living Cells. *Biophys. J.* **1997**, *73*, 653–658.
43. Shevchuk, A. I.; Gorelik, J.; Harding, S. E.; Lab, M. J.; Klenerman, D.; Korchev, Y. E. Simultaneous Measurement of Ca^{2+} and Cellular Dynamics: Combined Scanning Ion Conductance and Optical Microscopy to Study Contracting Cardiac Myocytes. *Biophys. J.* **2001**, *81*, 1759–1764.

44. Novak, P.; Li, C.; Shevchuk, A. I.; Stepanyan, R.; Caldwell, M.; Hughes, S.; Smart, T. G.; Gorelik, J.; Ostanin, V. P.; Lab, M. J.; *et al.* Nanoscale Live-Cell Imaging Using Hopping Probe Ion Conductance Microscopy. *Nat. Methods* **2009**, *6*, 279–281.
45. Takahashi, Y.; Murakami, Y.; Nagamine, K.; Shiku, H.; Aoyagi, S.; Yasukawa, T.; Kanzaki, M.; Matsue, T. Topographic Imaging of Convolved Surface of Live Cells by Scanning Ion Conductance Microscopy in a Standing Approach Mode. *Phys. Chem. Chem. Phys.* **2010**, *12*, 10012–10017.
46. Adenle, O. A.; Fitzgerald, W. J. Simulating Scanning Ion Conductance Microscopy Using a Monte Carlo Approach. *Scanning* **2006**, *28*, 79–80.
47. Edwards, M. A.; Williams, C. G.; Whitworth, A. L.; Unwin, P. R. Scanning Ion Conductance Microscopy: A Model for Experimentally Realistic Conditions and Image Interpretation. *Anal. Chem.* **2009**, *81*, 4482–4492.
48. Nitz, H.; Kamp, J.; Fuchs, H. A Combined Scanning Ion-Conductance and Shear-Force Microscope. *Probe Microsc.* **1998**, *1*, 187–200.
49. Rheinlaender, J.; Schäffer, T. E. Image Formation, Resolution, and Height Measurement in Scanning Ion Conductance Microscopy. *J. Appl. Phys.* **2009**, *105*, 094905.
50. Rheinlaender, J.; Schäffer, T. E. Scanning Ion Conductance Microscopy. In *Scanning Probe Microscopy of Functional Materials: Nanoscale Imaging and Spectroscopy*, 1st ed.; Kalinin, S. V.; Gruverman, A., Eds.; Springer: New York, NY, 2011; pp 433–460.
51. Chen, C. C.; Derylo, M. A.; Baker, L. A. Measurement of Ion Currents through Porous Membranes with Scanning Ion Conductance Microscopy. *Anal. Chem.* **2009**, *81*, 4742–4751.
52. Chen, C. C.; Baker, L. A. Effects of Pipette Modulation and Imaging Distances on Ion Currents Measured with Scanning Ion Conductance Microscopy (SICM). *Analyst* **2011**, *136*, 90–97.
53. Ebejer, N.; Schnippering, M.; Colburn, A. W.; Edwards, M. A.; Unwin, P. R. Localized High Resolution Electrochemistry and Multifunctional Imaging: Scanning Electrochemical Cell Microscopy. *Anal. Chem.* **2010**, *82*, 9141–9145.
54. Lai, S. C. S.; Dudin, P. V.; Macpherson, J. V.; Unwin, P. R. Visualizing Zeptomole (Electro)Catalysis at Single Nanoparticles within an Ensemble. *J. Am. Chem. Soc.* **2011**, *133*, 10744–10747.
55. Fleischer, R. L.; Price, P. B.; Walker, R. M. *Nuclear Tracks in Solids*; University of California Press: Berkeley, CA, 1975.
56. Siwy, Z.; Gu, Y.; Spohr, H. A.; Baur, D.; Wolf-Reber, A.; Spohr, R.; Apel, P.; Korchev, Y. E. Rectification and Voltage Gating of Ion Currents in a Nanofabricated Pore. *Europhys. Lett.* **2002**, *60*, 349–355.
57. Davenport, M.; Rodriguez, A.; Shea, K. J.; Siwy, Z. S. Squeezing Ionic Liquids through Nanopores. *Nano Lett.* **2009**, *9*, 2125–2128.
58. Korchev, Y. E.; Milovanovic, M.; Bashford, C. L.; Bennett, D. C.; Sviderskaya, E. V.; Vodyanoy, I.; Lab, M. J. Specialized Scanning Ion-Conductance Microscope for Imaging of Living Cells. *J. Microsc. (Oxford, U. K.)* **1997**, *188*, 17–23.